Transition from monolayer-thick 2D to 3D nano-clusters on α-Al 2 O 3 (0001)

Rémi Lazzari, Jacek Goniakowski, Gregory Cabailh, Rémi Cavallotti, Jacques Jupille, Nicolas Trcera, Pierre Lagarde

Journal Name

ARTICLE TYPE

Cite this: DOI: 00.0000/xxxxxxxxxx

Transition from monolayer-thick 2D to 3D nano-clusters on α-Al_2O_3(0001)

Rémi Lazzari,*[a] Jacek Goniakowski,[a], Gregory Cabailh[a], Rémi Cavallotti[a], Jacques Jupille[a], Nicolas Trcera[b], Pierre Lagarde[b]

Received Date
Accepted Date

DOI: 00.0000/xxxxxxxxxx

This paper reports on the long-standing puzzle of the atomic structure of the Ag/α-Al_2O_3(0001) interface by combining x-ray absorption spectroscopy, to determine Ag local environment [*i.e.* average Ag-Ag (d_{Ag-Ag}) and Ag-O (d_{Ag-O}) interatomic distances and Ag coordination numbers (CN)], and numerical simulations on nanometric-sized particles. The experimental key was the capability of a structural study of clusters involving only a few atoms. The concomitant decrease of d_{Ag-Ag} and CN with decreasing cluster size provides unambiguous fingerprints for the dimensionality of the Ag clusters in the subnanometric regime leading to a series of unexpected results regarding the size-dependent interface structures. At low coverage, Ag atoms sit on surface Al sites to form buckled monolayer-thick islands associated with a Ag-Ag distance (2.75 Å) which fits the alumina lattice. Upon increasing Ag coverage, as 3D clusters appear, the Ag interface atoms tends to leave Al sites to sit atop O atoms as d_{Ag-Ag} increases. The then highlighted size-dependent evolution, is built on structural models which seemed so far contradictory in a static vision of the interface. Theory generalizes the case as it predicts the existence of alumina-supported 2D clusters of Pd and Pt at small coverage and a similar 2D-3D transition upon increasing the size. The structural transformation from 2D Ag clusters to macroscopic 3D islands is accompanied by a noticeable reduction of adhesion energy at Ag/α-Al_2O_3(0001) interface.

1 Introduction

The crystallography of interfaces is an essential ingredient in the formation of supported nanoparticles. It governs the growth and the energetics of the particles and has therefore dramatic consequences on their adhesion, their morphology and related properties[1–3]. Interface structure determination is an ongoing challenge when studying metal/α-Al_2O_3(0001) systems, due to the complexity of the oxide surface which involves five types of sites [labelled Al_1, Al_2, Al_3, O and H (hollow) in Fig. 1]. These systems are of considerable interest as the α-Al_2O_3(0001) surface is the second most studied oxide surface after the (110) one of rutile TiO_2[4]. Since it is not reduced in contact with most transition metals[5–9], this surface offers a vast playground to explore sharp interface properties. Its attractiveness is increased by the countless applications of metal/alumina interfaces to catalysis[10–14], microelectronics[6] and functional coatings[15–21]. The question of the interface structure of epitaxial films on alumina reverberates also in the field of semiconductors such as GaN[22] or ZnO[23] and more recently of 2D materials[24,25].

The prerequisite of a knowledge of the interface structure has prompted a wealth of atomic first-principles simulations of metal-alumina systems. However, the similarity in binding energies of the metal adlayers associated to the different types of sites of the α-Al_2O_3(0001) surface[26] strongly complicates the optimization of the interface structures and prevents consensus. Ag[27–31] and Al[15,28,32,33] adatoms are mostly suggested to sit atop Al_3 but also atop O[28,34]. Ag has also been reported on hollow sites[15,32,35]. Isolated Pd[28,29,36–39], Pt[27,29,37,38] and Au[29,34,35] atoms are mainly found on O sites but have also been found atop Al[27,28,31,34,40]. As for multilayered Ag films, theoretical predictions that they sit either atop O or atop Al or on hollow sites[15,32,34] are not conclusive. Slab simulations raise an additional question in that, to make them tractable, the lattices of the metal and of the support are assumed to be matched and in registry at the interface. The imposed constraint[34] might affect the reliability of the conclusions reached especially as nanoparticles are involved. Nevertheless, some metal/α-Al_2O_3(0001) cluster calculations[30,31,39–41] can also be found. For the sizes which were explored (up to ten atoms), a tendency to form Ag, Pd and Au 2D clusters with metal adatoms atop Al sites

[a] *CNRS, Sorbonne Université, Institut des NanoSciences de Paris, UMR 7588, 4 Place Jussieu, F-75005 Paris, France.*
[b] *Synchrotron SOLEIL, L'Orme des Merisiers, Départementale 128, 91190 Saint-Aubin, France.*
* *Corresponding author, E-mail: remi.lazzari@insp.jussieu.fr*

is highlighted. The point is less clear when it comes to Pt. Soft landed Pt_n clusters were shown to lay flat on the surface up to $n = 18$ and form bilayered clusters above that value[42], whereas Pt_{10} islands have also been predicted to form bilayered structures[31,41].

In contrast to the abundance of *ab initio* calculations relating to the metal/α-Al_2O_3(0001) interface structures, the corresponding experimental investigations at the atomic scale are completely lacking, even if epitaxial orientations have been evidenced[43–45]. The challenge lies in the ability to explore nano-sized supported particles down to clusters of a few atoms on a bulk insulator which rules out the use of scanning tunneling microscopy as on metal-supported thin oxide films[10]. In atomic force microscopy, tip convolution[46] makes it difficult to determine the true nano-cluster shape and prevents revealing atomic scale details. Imaging by Transmission Electron Microscopy requires, beyond *in situ* deposition capabilities, a substrate preparation procedure that does not guarantee a surface termination similar to the bulk Al_2O_3(0001). Instead, it has been chosen herein to explore Ag/α-Al_2O_3(0001) by Extended X-ray Absorption Fine Structure (EXAFS). The authors have proved the flexibility and the reliability of this technique for studies on oxide-supported Ag[47–49], Na[50–52] and Cr[8,9], and on Ag-supported MgO nanoparticles[53], with a relevance even increased in the recent years by the systematic support of atomistic calculations[8,9,49,53]. As a local probe, EXAFS has several crucial advantages over imaging and diffraction experiments as it allows the *in situ* exploration of deposit conformation and environment for surface coverages as small as a tenth of a monolayer in the absence of long-range order. As regards the chosen Ag/α-Al_2O_3(0001) system, it is likely the metal/alumina interface which has concentrated the most important theoretical research efforts owing to its applicative interest in catalysis in particular for the major reaction of ethylene epoxidation[15,27–32,34,35]. In Ag clusters smaller than 2.5 nm in size (obtained for Ag equivalent thicknesses smaller than 0.4 nm), a shrinking of the interatomic distance d_{Ag-Ag} was previously interpreted as a trend for a matching of the metal lattice to that of the alumina substrate (see Fig. 3 of Ref. 49). The case prompted us to scrutinize the structure of Ag particles of size less than 2 nm in an attempt to observe this matching. To tackle the issue, the geometry of the Ag nanoparticles vapour-deposited on Al_2O_3(0001) under ultra-high vacuum has been experimentally determined by EXAFS at the Ag L_3-edge (see Section. 4). Then, the findings have been supplemented by atomistic simulations with the prospect that calculations based on experimental measurements of interatomic distances and coordination numbers can reliably lead to unambiguous solutions. Both experimental and theoretical methods are detailed in Sec. 4. The results obtained led us to revisit the entire Ag/alumina system in the light of the structural parameters accessible by EXAFS, and to discuss the change in adhesion energy at the metal-oxide interface as a function of cluster size.

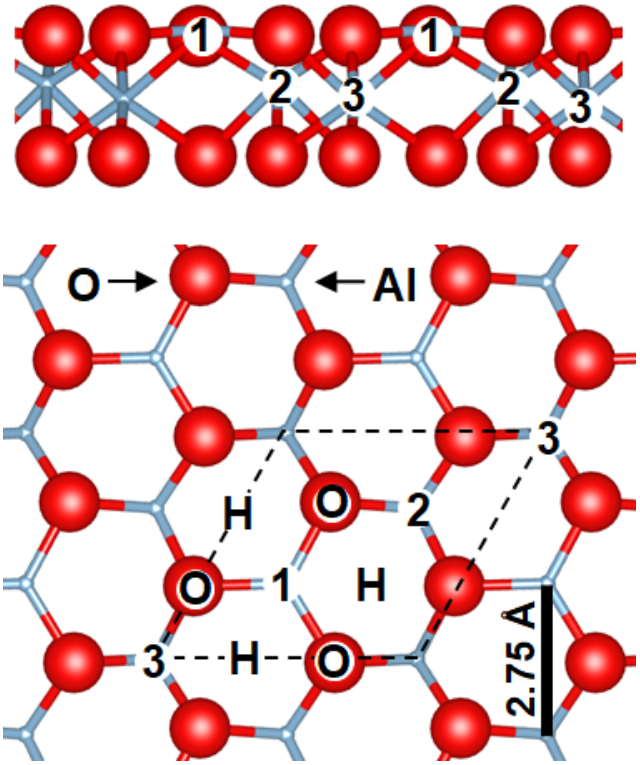

Fig. 1 Side and top views of the α-Al_2O_3(0001) surface. Oxygen and aluminum ions are shown by red and blue spheres, respectively. Al_1, Al_2, Al_3, O and H (hollow) sites are indicated. The bar stands for the characteristic distance of 2.75 Å between surface sites and the dotted line for the surface unit cell.

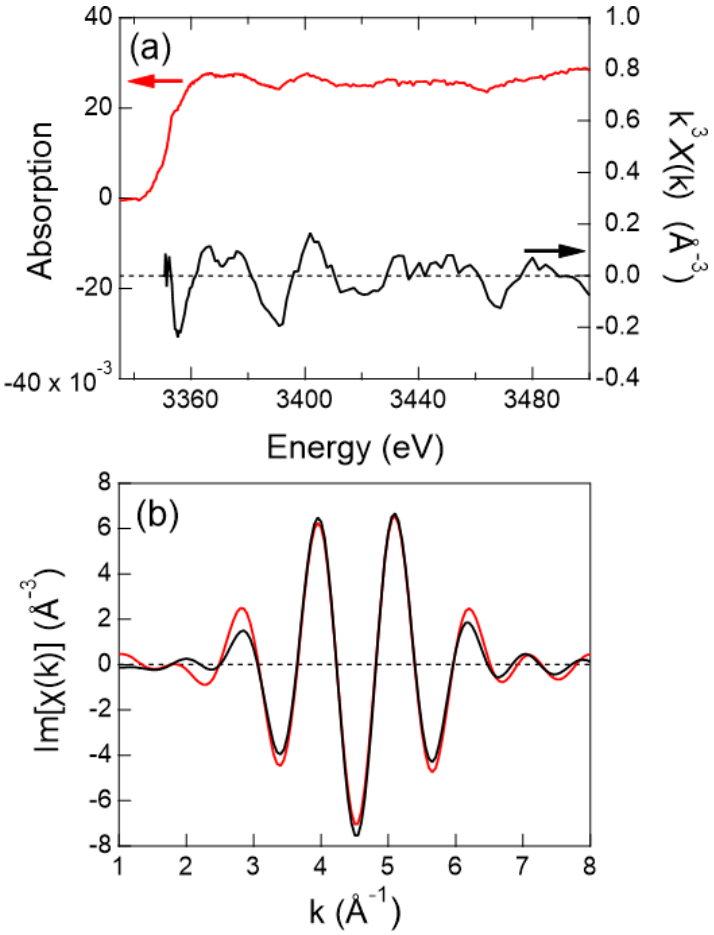

Fig. 2 EXAFS result and analysis for one of the deposits analysed herein (large cross in Figure. 4-a): (a) Raw experimental absorption spectrum (red line) where the pre-edge background has been removed and the corresponding EXAFS data (black line). Note that this spectrum uses the same energy scale than the absorption data and not the usual k wave vector. (b) The Fourier filtered experimental data (red line) and the result of the EXAFS fit (black line) which returns 6 ± 1.5 Ag atoms at a distance of 2.77 ± 0.025 Å.

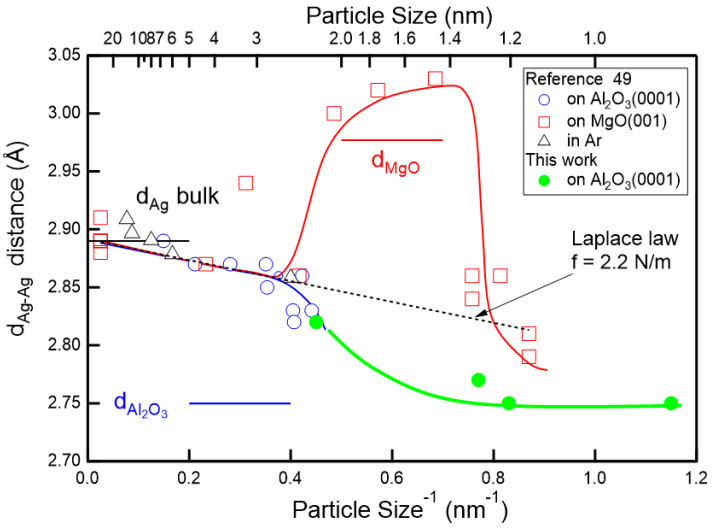

Fig. 3 Ag-Ag distance d_{Ag-Ag} in Ag clusters as a function of the inverse of the particle size D^{-1}. For comparison with the present work of Ag/α-Al_2O_3(0001) (green circles and green line), the figure reproduces the data shown in Fig. 3 of Ref. 49: Ag supported on MgO(001) (red squares and red line), α-Al_2O_3(0001) (blue circles and blue line) and Ag clusters embedded in Ar (black triangles). The dashed black line corresponds to the macroscopic Laplace rule[49,54] $\frac{\Delta d_{Ag}}{d_{Ag(bulk)}} = \frac{4}{3}\frac{fK}{D}$ that links the strain induced by the surface stress f in a particle of size D to the bulk compressibility K; the slope gives the value $f = 2.2$ N.m^{-1} for silver. The blue, red and green continuous lines are to guide the eyes. Ag, MgO, and Al_2O_3 characteristic bulk interactomic distances are shown by horizontal lines.

2 Results and discussion

2.1 EXAFS analysis

To complement the previous x-ray absorption measurements on Ag/α-Al_2O_3(0001) in which the smallest studied cluster size was slightly larger than 2 nm, corresponding to Ag coverage of about 0.06 nm[49], the present work has explored the behaviour of Ag films down to a coverage of 0.012 nm corresponding to about 0.05 monolayer of Ag(111), until reaching the limit of observability of the Ag L_3-edge. The ability to determine by EXAFS the structural parameters of clusters involving a few atoms in a sufficiently precise way to allow an unequivocal comparison with the DFT calculation is the key to the present experiments. As in previous data, the near-edge structure indicates that Ag is in metallic form whatever the coverage[49]. Ag-Ag distances d_{Ag-Ag} were determined by the analysis of both the imaginary part and the magnitude of the Fourier transform of the fine structure function $k^3\chi$(k) (Fig. 2). In parallel to previous findings[49], the found values (Tab. 1) are reported in Fig. 3 (green circles) as a function of the inverse of the particle size D^{-1} determined in a way which deserves some comments. As it will be shown below that very small Ag particles are in the form of 2D islands, the description of their size by the same parameters as in the 3D form is irrelevant. To compare with previous data, the size of the particles studied herein was determined through the cube root of the Ag thickness assuming similar particle densities. The series of new data is normalized with respect to the previous one thanks to the experimental point $d_{Ag-Ag} = 2.82$ Å common to the two series of measurements. Consequently, it is placed at $D^{-1} = 0.42$ nm^{-1}. The validity of the representation will be commented in the discussion. The evolution of d_{Ag-Ag} suspected in the previous study[49] is indisputably confirmed. The distance d_{Ag-Ag} deviates from the Laplace rule, that links overpressure and strain induced by surface stress in a nanoparticle[49,54], until reaching 2.75 Å, a value which is apparently dictated by the interatomic spacing characteristic of the α-Al_2O_3(0001) surface (Fig. 1). This transition of strain dominated by surface and then epitaxial stress parallels the behaviour of the Ag/MgO(001) interface[49] for which the bulk misfit is of opposite sign (-5.1 % vs 3 %) and the symmetry is different (hexagon/hexagon vs cube/cube) (Fig. 3).

The present findings give the whole Ag/α-Al_2O_3(0001) data set a new meaning that encourages further consideration of two other parameters derived from the EXAFS analysis, the coordination number of the Ag atoms CN and the Ag-O distance d_{Ag-O}

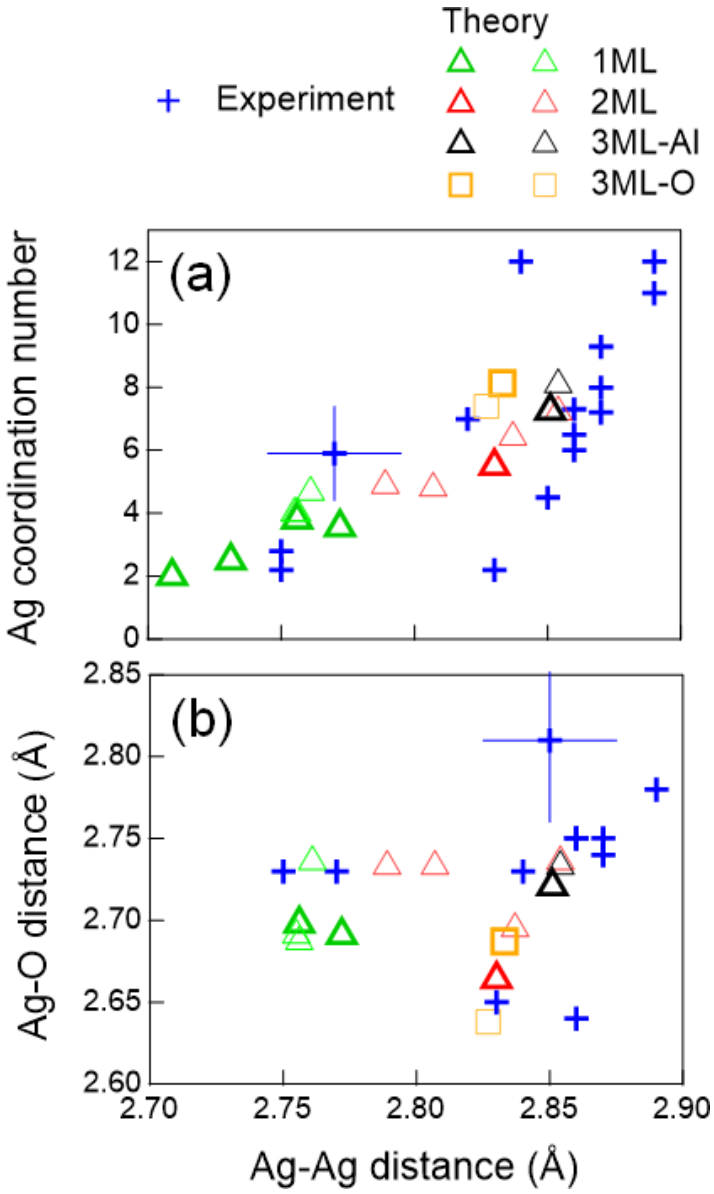

Fig. 4 Comparison between EXAFS measurements (blue crosses) and atomistic simulations related to Ag/α-Al_2O_3(0001) clusters: (a) coordination number of Ag (CN) and (b) d_{Ag-O}, as functions of d_{Ag-Ag}. Calculated values, represented by triangles, correspond to different cluster thicknesses: 1 ML (green); 2 ML (red); 3 ML in Al configuration (black) and in O configuration (orange). Bold symbols correspond to the isomers of highest stability. Typical experimental error bars are indicated in each figure.

(Fig. 4). All the data presented here as well as those collected previously[49] but not analysed at that time are now considered. The evaluation of d_{Ag-O} is made difficult by the vicinity of d_{Ag-Ag}. In the EXAFS signal, the Ag-O distance mostly manifests itself by a broadening of the Fourier transform even if it gives rise in some cases to a component that can be resolved (see Fig. 1-a of Ref. 49). The determination of d_{Ag-O} assumes that the shortest distances, *i.e.* those which are measured on the Al_3 site, dominate the EXAFS signal. Moreover, it must be ensured that the d_{Ag-O} distance is not confused with d_{Ag-Al}. Setting an Ag adatom on the Al_3 site, at a distance of 2.73 Å from the three surrounding oxygen atoms (Fig. 1), leads to a Ag-Al distance of 3.11 Å. Then a fit of a 0.017 nm thick film dataset where the d_{Ag-Ag} and d_{Ag-O} distances are fixed (2.89 Å and 2.73 Å, respectively) returns consistently a value of 3.11 Å for the Al neighbours. This supports the present assignment of 2.73 Å to Ag-O bonds.

As seen in Fig. 4-a, the decrease in coordination number is concomitant with the decreases in d_{Ag-Ag}. Bearing in mind that the bulk Ag CN is 12, the lowest values found between 2 and 3 reveal the existence of very small objects whose shape cannot be described based on EXAFS data alone but requires calculations. As regards to d_{Ag-O}, the evolution of the widely scattered experimental values can hardly be rationalized by simple inspection. However, some confidence can be placed in these data as they show similar trends as atomistic calculations developed below (Fig. 4-b, blue crosses versus other symbols).

2.2 Ag/α-Al_2O_3(0001) structure from DFT

To get insight into the microscopic effects responsible for the measured structural parameters of small Ag particles, DFT calculations have been performed on series of model supported Ag clusters. First, attention was focused on larger Ag particles and the structural signature that distinguishes the two competing interface configurations, namely Ag either on surface O atoms or surface Al atoms, was analyzed. Then, the structure of the smallest Ag clusters (composed of less than 12 atoms), in both 2D and 3D forms were directly compared to experimental data, in terms of d_{Ag-Ag}, d_{Ag-O} and CN (Tab. 1).

2.2.1 Interface configurations

As a first step, supported face-centred cubic (fcc) Ag particles have been considered in the form of truncated octahedra composed of either 73 (Ag_{73}) or 43 (Ag_{43}) atoms, which belong to the series of epitaxial clusters Ag(111)/Al_2O_3(0001) in the scalable regime of size described in Ref. 49. The two retained cluster sizes gave aggregates with balanced profiles for which it was possible to stabilize two distinct interface configurations, with Ag atoms in either Al-top (Al_1, Al_2, Al_3) or O-top (O) sites of the alumina surface, while the hollow (H) sites did not produce a local energy minimum (Fig. 5).

The two relaxed interfaces display quite distinct structural characteristics. As O-top surface sites are all equivalent, clusters in O configuration preserve regular bulk-like fcc structures with quasi-planar atomic (111) layers. Small distortions take place at the very cluster edges only. In the absence of any pronounced

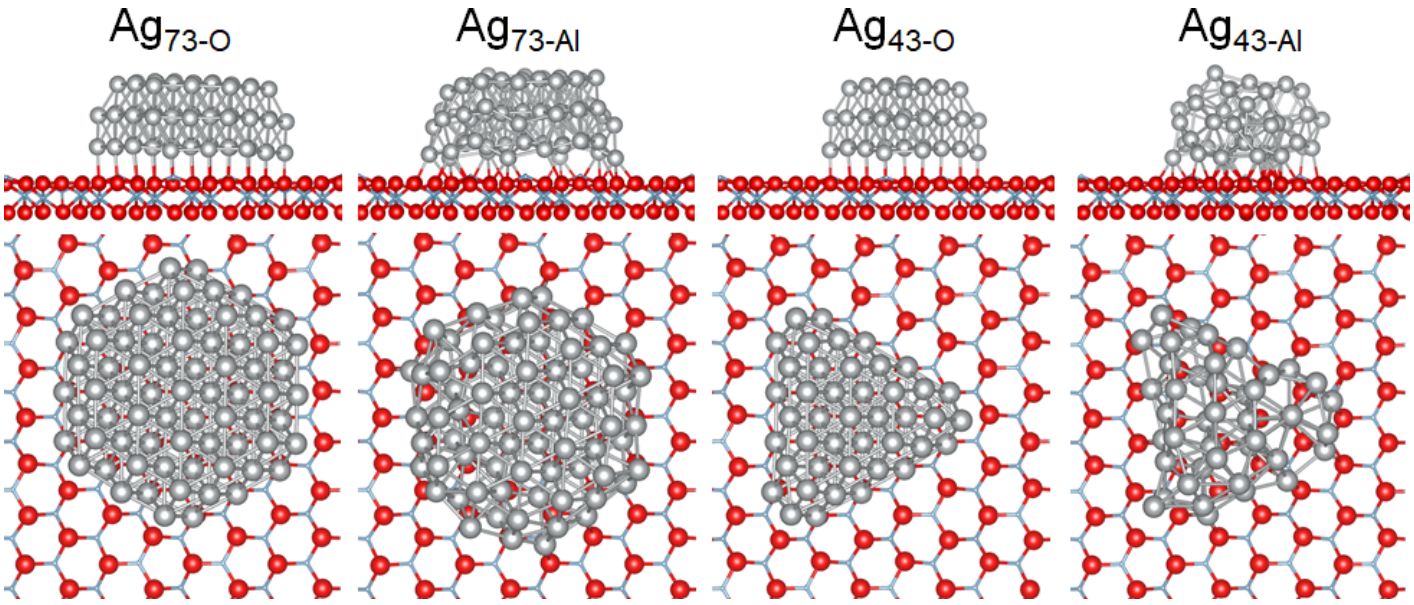

Fig. 5 Side and top views of the Ag_{73} and Ag_{43} clusters in either the O or the Al interface configuration. Same color code as in Fig. 1 with Ag atoms as grey spheres.

distortions, d_{Ag-Ag} distances are homogeneously distributed with an average value (2.83 Å) close to that in the corresponding free particles (2.81-2.83 Å, Tab. 1). Short average interfacial d_{Ag-O} distances are found, which decrease as the particle gets smaller (2.69 and 2.64 Å for Ag_{73-O} and Ag_{43-O}, respectively). In contrast, clusters in the Al interface configuration undergo a pronounced structural distortion driven by the strong inequivalence of the surface Al sites with in particular the presence of protruding surface Al for every third atom (Fig. 1); the distortion is not limited to the interface layer but propagates throughout the entire particle. This configuration corresponds to the often described buckled Ag/α-Al_2O_3(0001) adlayer which accounts theoretically for the different heights at which Al_1, Al_2 and Al_3 are located with respect to the alumina surface (Fig. 1)[27,28,31,34,40]. It results in a non-negligible expansion of the average Ag-Ag distances (2.85 Å) and in substantially longer and little size-dependent average Ag-O bond lengths (2.72-2.73 Å).

These structural signatures can be now compared to the measurements relative to the small Ag particles ($D^{-1} \geq 0.6$ nm^{-1} in Fig. 3). Regardless of the particle size and the precise interface configuration, the calculated average d_{Ag-Ag} distances in 3D supported clusters (2.83-2.85 Å) do not match measurements (~ 2.75 Å) at all. Also, average d_{Ag-O} distances calculated for the O interface configuration (2.64 and 2.69 Å for the two clusters) are much shorter than the experimental estimates. Conversely, the good agreement with the measurements of the d_{Ag-O} distances calculated for the Al configuration (2.73 Å) is a strong indication that the small Ag particles observed herein adopt this configuration.

At this point, it is worth noticing that, while both O and Al configurations produce local minima of the total energy, their relative stability depends on the cluster size. The Al interface configuration is 0.6 eV more stable in the smaller Ag_{43} cluster, but it is 0.6 eV less stable in the Ag_{73}. This calculated stability reversal as a function of cluster size can be assigned to two main effects, the energy cost of cluster distortion and the energy gain induced by the associated enhancement of cluster-substrate interaction. The former increases as the cluster size increases (+2.1 eV and +2.5 eV for Ag_{43} and Ag_{73} clusters, respectively) and tends to prohibit distortions in larger particles. The latter, weakens as a function of the cluster size (−2.7 eV and −1.9 eV, for Ag_{43} and Ag_{73} clusters, respectively) since smaller particles, being more flexible, better adapt to the substrate. These effects favour the distorted Al interface configuration in smaller particles (and, as it will be demonstrated in the following, also in the flatter ones) and show that the larger clusters (but also more 3D-shaped ones) will tend to adopt the O-top configuration and preserve their quasi-undistorted (111) structure.

The shift from Al sites to O sites sheds light on the puzzling variations of Ag-O interatomic distances (Fig. 4-b). Upon increasing the size of Ag nanoparticles, the transition from more flexible 2D islands sitting atop Al to stiffer 3D clusters in an O interface configuration is accompanied by a shortening of Ag-O distances. Therefore, a dip in d_{Ag-O} in both experimental and theoretical values is consistently observed around $d_{Ag-Ag} = 2.83 - 2.86$ Å. At higher coverages, the gradual expansion of the average Ag-O distance is attributed to an increase in lattice mismatch at the interface between larger clusters and the alumina surface. Compared to previous work, this corresponds to the appearance of a lattice mismatch between Ag and alumina, *i.e.* to the transition from zone I to zone II in Fig. 2-c of Ref. 49.

However, the present results also show unexpected changes in Ag sites with Ag interface atoms sitting either atop surface Al atoms or atop surface O atoms. Most importantly, the structural models associated to these different sites are demonstrated to actually exist whereas they were considered as conflicting until now.

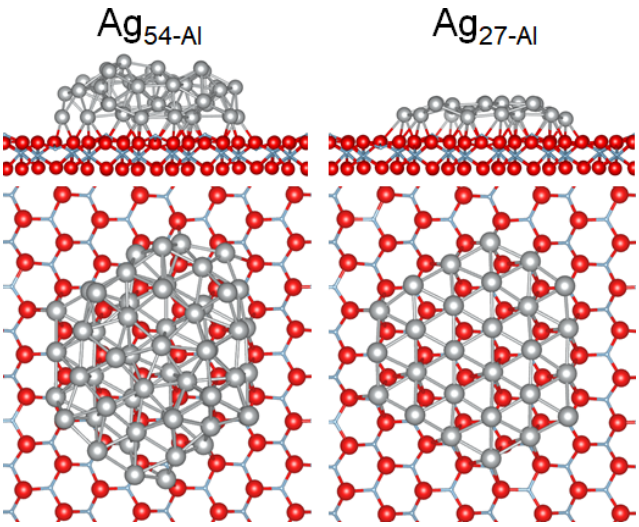

Fig. 6 Side and top views of the Ag_{54} and Ag_{27} clusters in the Al interface configuration. Same color code as in Fig. 5.

2.2.2 Effect of cluster thickness

In a second step, either one or two top-most Ag layers were removed from the Ag_{73-O} cluster, as to produce flatter, 2- and 1-layer-thick, Ag_{54} and Ag_{27} particles, respectively (Fig. 6). These two flatter clusters spontaneously relax into the Al configuration and could not be stabilized atop O sites. The similarity of the average Ag-O distances (2.74 Å) with those calculated above for the Al configuration in the 3D particles confirms the robustness of this structural signature. The preference for the Al configuration can be linked to the combination of a lower energy cost of structural distortions in flatter particles and a better access to the favourable Al_3 site.

However, the calculated Ag-Ag distances in the two particles differ significantly. For the 2 ML thick Ag_{54-Al}, d_{Ag-Ag} (2.85 Å) is close to what is obtained for 3D clusters (Tab. 1). In stark contrast, the particularly short value associated to the 1-layer-thick Ag_{27-Al} cluster (2.76 Å) matches nearly perfectly the experimental estimates associated to the smaller Ag particles. Thus, it becomes clear that the 1-layer-thick particles with Ag atoms atop the Al sites of the alumina surface provide the unique satisfactory match with the measured structural parameters associated with the smallest observed Ag deposits.

2.2.3 Effect of cluster size

Finally, small Ag clusters were simulated to explore how the structural signatures discussed above behave upon a reduction of the particle size. Here we will describe more thoroughly the Ag_9 and Ag_{12} clusters for which we were able to stabilize regular low energy isomers of both 1 ML (2D) or 3D forms (Fig. 7). Data for Ag_3, Ag_4, and Ag_{10} particles are also reported in Tab. 1. In 3D Ag_9 and Ag_{12} particles, the d_{Ag-Ag} distances (2.79 and 2.83 Å, respectively) tend to approach the values found in thicker 3D (2 ML and 3 ML) particles (2.83-2.85 Å). Conversely, the two 2D clusters display a short average Ag-Ag distance (2.77-2.75 Å) close to those found in larger 1 ML clusters (2.76 Å), but much longer than those predicted (2.65-2.67 Å) for free Ag_3 to Ag_6 2D clusters (Tab. 1 and Refs. 55,56). Being observed neither for free 2D particles nor for 3D particles whether free or supported, the specific measured value of the d_{Ag-Ag} distance ($\sim 2.75-2.77$ Å) is therefore a robust and reproducible structural signature for 1 ML thick α-Al_2O_3(0001)-supported Ag particles with interface atoms sitting on Al sites of the alumina surface. Moreover, the good agreement of the theoretical and experimental values of the coordination number CN represented as a function of the distance d_{Ag-Ag} shows that this distance is systematically linked to the dimensionality of the particles (Fig. 4-a). Indeed, beyond the general impression of a monotonous increase of CN as a function of d_{Ag-Ag}, a closer inspection reveals that values are gathered by zones. For alumina-supported 2D Ag islands from 3 to 27 atoms, values of d_{Ag-Ag} do not exceed 2.76-2.77 Å, even for large islands, while, for 2 ML-thick particles, they belong to a higher range starting at 2.79-2.81 Å, even for very small objects (Tab. 1 and Fig. 4-a). The dramatic changes in the Ag/α-Al_2O_3(0001) interface structure which accompany the increase in Ag coverage are therefore unequivocally associated with defined cluster thicknesses and defined cluster sizes.

In light of the above computational estimation, the actual size of the observed supported 1 ML islands deserves a comment. In fact, the smallest experimental coverage of 0.05 Ag(111) monolayer (0.012 nm), *i.e.* 7×10^{13} Ag atoms.cm^{-2} leads to the reasonable estimate[57] of 7×10^{12} aggregates.cm^{-2} by assuming clusters of ~ 10 atoms in line with the above calculations. The value of $D^{-1} = 1.1$ nm^{-1} assigned to this data point in Fig. 3 via the cube root of the Ag thickness makes sense although it is perhaps underestimated. However, the highest coverage of 0.04 nm (2.3×10^{14} atoms.cm^{-2}) at which 2D clusters are experimentally evidenced herein (Fig. 3) might corresponds to particles of several tens of atoms within the common density limit of 1×10^{13} aggregates.cm^{-2}[57]. Their structural parameters d_{Ag-Ag} (2.75 Å) and d_{Ag-O} (2.73 Å) show unambiguously that they are 1 ML-thick, which highlights that such large 2D islands can actually form at the surface of α-Al_2O_3(0001). Several factors may favour such large 2D islands, including the existence of magic number clusters[58–60], the partial fragmentation of islands[58], presence of surface defects, not to mention kinetic effects during cluster growth.

2.3 Interplay between metal-metal and metal-alumina interaction

The above comparison between the experimental and calculated structural characteristics points clearly to the existence of 1 ML-thick clusters on the alumina surface. To complement the picture, in the following, the relative stability of the supported Ag particles is analysed as a function of their size and their 2D/3D character, taking as an example the Ag_9 and Ag_{12} particles represented in Fig. 7.

It is found that the 2D shape is favoured (by 0.03 eV/Ag) in the case of the Ag_9 particle, whereas the Ag_{12} cluster is more stable (by 0.03 eV/Ag) in the 3D shape. This suggests an inversion of the relative thermodynamic stability between the

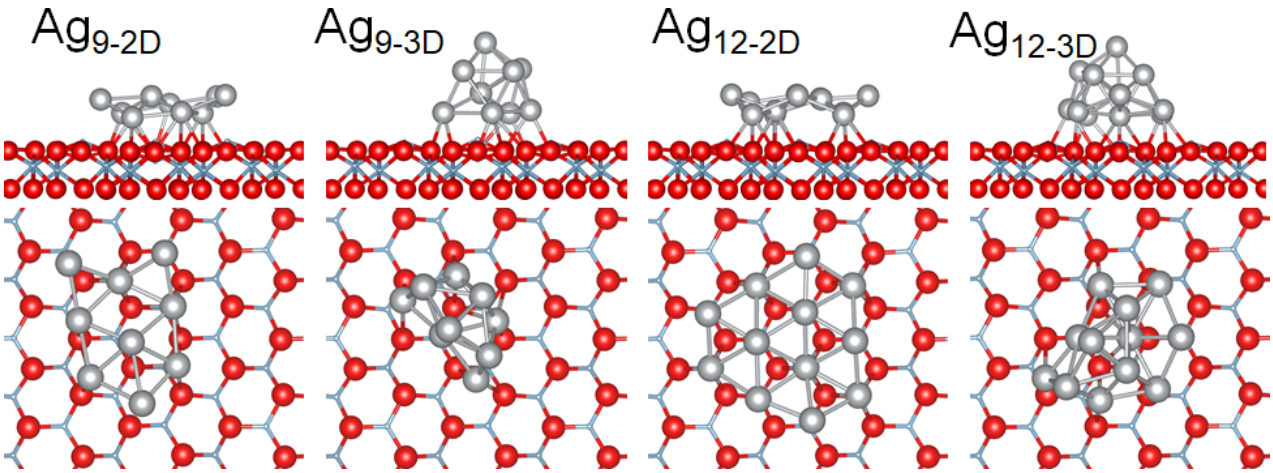

Fig. 7 Side and top views of the Ag_9 and Ag_{12} clusters in 2D (1 ML) and 3D configurations. Same color code as in Fig. 5.

Systems		Thickness (nm)	d(Ag-Ag) (Å)	Coord. number	d(Ag-O) (Å)
Experimental data		0.012	2.75	2.2	
		0.032	2.75	2.8	2.73
		0.04	2.77	5.9	2.73
		0.2	2.82	7	
DFT alumina-supported Ag clusters	Stability	Size and shape			
	More stable isomers	Ag_{73-O} (3 ML)	2.83	8.1	2.69
		Ag_{43-Al} (3 ML)	2.85	7.3	2.72
		Ag_{12-Al} (2 ML)	2.83	5.5	2.66
		Ag_{10-Al} (1 ML)	2.76	3.8	2.70
		Ag_{9-Al} (1 ML)	2.77	3.6	2.69
		Ag_{4-Al} (1 ML)	2.73	2.5	2.55
		Ag_{3-Al} (1 ML)	2.71	2.0	2.40
	Less stable isomers	Ag_{73-Al} (3 ML)	2.85	8.1	2.73
		Ag_{43-O} (3 ML)	2.83	7.4	2.64
		Ag_{54-Al} (2 ML)	2.85	7.2	2.74
		Ag_{10-Al} (2 ML)	2.81	4.8	2.73
		Ag_{9-Al} (2 ML)	2.79	4.9	2.73
		Ag_{27-Al} (1 ML)	2.76	4.7	2.74
		Ag_{12-Al} (1 ML)	2.75	4.0	2.69
DFT free Ag clusters		Ag_{79} (3D)	2.83	8.5	–
		Ag_{43} (3D)	2.81	7.3	–
		Ag_{13} (3D)	2.80	5.7	–
		Ag_6 (1 ML)	2.67	3.0	–
		Ag_5 (1 ML)	2.67	2.8	–
		Ag_4 (1 ML)	2.66	2.5	–
		Ag_3 (1 ML)	2.65	2.0	–

Table 1 Summary of the experimental and calculated structural characteristics of free and $\alpha-Al_2O_3(0001)$ supported clusters.

Metal		Ag	Pd	Pt
Cluster size and	M_9	2D	2D/3D	2D
dimensionality	M_{12}	3D	3D	2D
Interaction	M-M	0.1	0.4	0.2-0.3
strength (eV)	M-A	0.4-0.6	1.2	1.0

Table 2 Energetically favoured shapes of 9- and 12-atom-large alumina-supported Ag, Pd, and Pt clusters. The interplay between the metal-metal (M-M) and metal-alumina (M-A) interaction strengths drives the progressive transition between favoured 2D (smallest particles) and 3D (larger ones) particle shapes (3D shapes are systematically favoured in the corresponding freestanding particles).

two types of particles at the size of about 10 atoms, consistently with the existing computational evidence[31] and with the present experimental indication on the existence of a variety of 1 ML-thick clusters. The good stability of small 2D Ag particles is to be principally assigned to the small cost of 3D $\rightarrow$ 2D shape transformation in the corresponding unsupported Ag clusters (obtained by relaxing the supported ones once the substrate is removed). Indeed, for the considered 9- and 12-atom-large particles, it amounts to about 0.7 eV, which corresponds to only 0.1 eV per Ag-Ag bond broken upon such transformation. Since this energy cost is to be compared to the energy gain due to the additional Ag-alumina interaction ($\sim 0.4-0.6$ eV/Ag atom at the interface, see Tab. 2) the 2D form is favoured as long as it does not imply a massive loss of Ag-Ag bonds.

With the help of the same 9- and 12-atom-large clusters, similar effects are found for alumina-supported Pd and Pt (Tab. 2). However, compared to Ag, the energy cost of 3D $\rightarrow$ 2D transformation is much larger in Pd clusters (about 0.4 eV per broken Pd-Pd bond) and it is only partially compensated by the larger Pd-alumina interaction energy (1.2 eV/Pd-O bond at the interface, Tab. 2). As a consequence, 3D Pd particle shapes are favoured starting already for smaller sizes. Conversely, in the case of Pt clusters, the loss of Pt-Pt interaction (0.2-0.3 eV/Pt-Pt bond) is fairly well compensated by the Pt-alumina one (1.0 eV/Pt-O bond at the interface, Tab. 2) which favours 1 ML clusters over a larger span of sizes. The prediction is consistent with the observation that soft landed Pt_n clusters form 2D islands up to $n = 18$[42].

2.4 Adhesion energy of Ag/α-Al_2O_3(0001)

The evolution of presently calculated adhesion energies of the most stable clusters [0.34, 0.39, 0.52, 0.74, and 0.81 eV/Ag for Ag_{73-O}, Ag_{27-Al}, Ag_{12-Al}, Ag_4, and Ag_3 clusters, respectively, which, by assuming $d_{Ag-Ag} = 2.75$ Å, span energies from about 0.8 J.m^{-2} (Ag_{73}) up to nearly 2.0 J.m^{-2} (Ag_3)] qualitatively confirms the trend evidenced in previous analysis of the morphology of supported metal particles[49,57,61] by plasmonics[62–64]. On this same Ag/alumina system[49] and also on a whole series of metal/dielectrics systems[61], a "U" shaped evolution of the aspect ratio of the particles with their sizes was evidenced. Those studies highlight a progressive increase of the adhesion energy of supported particles upon decreasing size in the range $\lesssim$ 10 nm in which particles, that no longer show self-similar profiles observed at the mesoscopic scale, escape the current analytic models[13,65]. The domain is particularly crucial because it involves particles whose dimensions are optimal with respect to many properties[13,58,66,67].

3 Conclusion

This work dealt with the long-lasting puzzle of the interface structure of the Ag/α-Al_2O_3(0001) interface at the atomic level by combining x-ray absorption spectroscopy with atomistic simulation. The study reveals a size-dependent interface structure involving changes in dimensionality of the supported clusters which are unambiguously linked to the Ag-Ag and Ag-O interatomic distances and the Ag coordination number. At low coverage, Ag forms buckled 2D islands sitting on Al sites. Upon increasing coverage, as clusters becomes 3D, Ag atoms move toward atop O positions. Overall, the present findings draw an unexpected evolution of the α-Al_2O_3(0001)-supported Ag clusters. Interface structure and energy, cluster thickness and size vary together with increasing Ag coverage. Theory predicts a similar behaviour for alumina-supported Pd and Pt nanoparticles. All these results ask the reason of the puzzling behaviour in the small size regime of the Ag/MgO(001) interface for which the metal/oxide interaction, the symmetry, the absorption site and the misfit are different. The present study reveals a hitherto never explored behaviour of supported metal clusters in the range of size $\lesssim$ 10 nm which is of paramount importance as it is optimal with respect to many properties.

4 Methods

Experiments have been performed on the LUCIA beamline at synchrotron SOLEIL (Saint-Aubin, France)[68] in an ultra-high vacuum (UHV) apparatus. The main chamber (base pressure 1×10^{-10} mbar), equipped with a Low-Energy Electron Diffraction (LEED) device and an Auger spectrometer (AES) to control the sample quality, is isolated from the beamline by a 7 μm thick Be window which allows to keep UHV during the experiments. Given the very high flux (around 10^{11} photons.s^{-1}.eV^{-1}) delivered by the Si(111) double crystal monochromator, a good signal-to-noise EXAFS spectrum on very thin deposits is obtained within two hours, by monitoring the total electron yield of the sample normalized by the upstream drain current on a thin Ni film (50 nm on a 2 μm polypropylene support). The focusing of the beam to a few micrometers allows grazing incidence spectra ($\sim 60^\circ$ from normal) without any loss of flux. This main experimental chamber is coupled to a preparation chamber and a load-lock system, which makes the whole set-up a very unique system for spectroscopic studies in the soft x-ray range.

Sample carbon contamination was removed in the preparation chamber by annealing at 1200 K in front of a doser[69] under an equivalent pressure of oxygen of about 10^{-4} mbar. The crystallographic quality of the substrate and its cleanliness were checked in the main chamber by LEED and AES. As expected from polarity consideration[70] and theoretical surface phase diagram[71], such a preparation procedure leads to an Al-terminated

(0001) surface; as in atomistic calculations, previous surface diffraction experiments[72,73] evidenced a strong inward relaxation of this terminal plane. Then, Ag has been deposited in the preparation chamber on the surface at room temperature by means of an effusion source at a rate of ca. 0.1 nm.minute^{-1} calibrated by a quartz microbalance. As small coverages of less than 0.4 nm down to about 0.01 nm were explored, the film thickness (as indicated hereafter) has been determined via the relative jump at the Ag L_3-edge $\delta I/I$ calibrated on a thick (3 nm) evaporation on the same substrate. The good linear regression of slope 0.85 between this procedure and the direct calibration by evaporation time shows an overall agreement within 20%.

Ag-covered samples were transferred to the main chamber to perform EXAFS measurements. All x-ray absorption spectra have been recorded around the Ag L_3-edge by monitoring the total electron yield recorded from the sample in the 3330-3530 eV energy range at normal and grazing incidences. The recorded EXAFS signal averages typically 6 scans with a dwell time of 1 second per point. The high-quality of the EXAFS data (Fig. 2) that were recorded allowed the analysis of extremely small amounts of deposited Ag less than 0.05 monolayer, as defined by the atomic density of the Ag(111) plane (1.38×10^{15} Ag atoms.cm^{-2} *i.e.* 2.35 Å). Spectra have been processed by the ATHENA-ARTEMIS suite[74] to extract the absorption modulations $\chi(k)$ (k electron wave vector) and then to obtain the structural parameters. An analysis of pure Ag metal of known atomic structure has first allowed to set the energy edge shift $E_0 = 3355.9$ eV and the so-called $S_0^2 = 0.6$ parameter. These values have been kept constant for all spectra, as well as the k-domain of the forward Fourier Transform ($1-6$ Å^{-1}) and the R-domain of the back filtered data ($1.7-3.6$ Å). The phase shift functions from Ag metal and Ag_2O were used in the ARTEMIS procedure. The fits returned, as usual, the interatomic distances, the coordination numbers and the disorder parameters which typical error bars are displayed in Fig. 2. For all spectra, the order of magnitude of the obtained Debye-Waller factor for the Ag-Ag pair and of the fit reliance factor were similar to those of Fig. 2 ($\sigma^2 = 0.015$ and $R = 0.04$, respectively). As usual for studies at the L-edge, the $p \rightarrow s$ transition has been neglected. In addition, as it would change the results by an amount smaller than the experimental errors, the effect of the photon beam polarization on the coordination number for these very small clusters has been ignored.

Compared to the Ag K-edge, the choice of the L_3-edge with its limited k-range of ~ 6 Å^{-1} due to the nearby L_2-edge deserves some comments. To account for this rather short domain, the error bars on parameters are not, in terms of interatomic distances or coordination numbers, those usually achieved in EXAFS nowadays at the K-edge of heavy elements (k-range up to ~ 12 Å^{-1}). But these values do not affect the conclusions of the present analysis which does not have to discriminate between close solutions. Notably, our first experiments on Ag/MgO(001) clusters performed at the Ag L-edge[47] (LURE, Laboratoire pour l'Utilisation de Rayonnement Electromagnétique) showed that Ag was sitting atop O on MgO(001) at a Ag-O distance of 2.53 Å, a result latter confirmed by grazing x-ray diffraction within 0.01 Å[75]. Further experiments were done at the Ag K-edge (ESRF, European Radiation Synchrotron Source, GILDA beamline)[48]. At 25.5 keV, the EXAFS signal taken in fluorescence, which dies out very rapidly beyond the edge, is strongly perturbed by the Compton effect of the substrate made of light elements, even for a very thin one, rendering the analysis of EXAFS data unreliable for small deposits as studied herein. In addition, the total electron yield is very low at these large photon energies. So, as both edges gave comparable results for Ag/MgO(001) deposits of similar thickness, the use of K-edge, despite a wider accessible k-range, would definitely not improve the experimental data in the present Ag/α-Al_2O_3 case.

All calculations regarding the Ag/α-Al_2O_3(0001) system were performed within the framework of the Density Functional Theory (DFT) approach implemented in the Vienna Ab-initio Simulation Package (VASP)[76,77]. Electron-core interaction was represented with the Projector Augmented Wave (PAW) method[78,79], with help of pseudopotentials provided with the package. The alumina substrate was represented by an Al-terminated slab composed of four Al-O_3-Al trilayers and the Ag clusters were deposited on its top side. A large (4×4)-Al_2O_3(0001) surface unit cell was used and the Brillouin zone was sampled with a single Γ point. All atomic coordinates of anions, cations, and deposited Ag atoms have been allowed to fully relax until forces got lower than 0.01 eV.Å^{-1}, apart from the bottom-most Al layer which was kept in its bulk position. The addition of a fifth oxide trilayer layer resulted in only negligible corrections to the reported quantities. Atomic configurations were plotted with VESTA[80].

Since the main goal of the present study is a fine analysis of the measured Ag-Ag (and, to a lesser extent Ag-O) distances, the PBEsol exchange-correlation functional[81] has been chosen. In stark contrast to the most frequently used GGA functionals, such as the PBE and PW91 ones, which tend to largely overestimate both the silver lattice parameter a and the bondlength in the free Ag_2 dimer d (up to about $a = 4.15$ Å and $d = 2.59$ Å, compared to the experimental values of $a = 4.09$ Å and $d = 2.53$ Å[82]), the much more satisfactory estimations obtained with the PBEsol ($a = 4.07$ Å, $d = 2.53$ Å) make a direct comparison of the measured and calculated Ag-Ag distances reliable. It is worth noting that the dispersion-corrected exchange-correlation functional (optB88-vdW)[83–85] reproduces well the behaviour of the Ag-Ag distances obtained from PBEsol calculations with, however, systematically 0.05 Å longer bonds. This is consistent with larger values of $a = 4.14$ Å and $d = 2.57$ Å predicted by the optB88-vdW functional. On the other hand, the explicit account for the van der Waals forces enhances the Ag-Al_2O_3(0001) interaction strength by about 0.1 eV/Ag, similarly to the effect reported for the Ag/MgO(001) system[86].

Conflicts of interest

There are no conflicts to declare.

Acknowledgements

This work benefited from the technical support of D. Roy (SOLEIL). R. Cavallotti PhD thesis was supported by a CIFRE grant form Arcelor-Mittal company.

Notes and references

1 C. Campbell, *Surf. Sci. Rep.*, 1997, **27**, 1–111.
2 C. Henry, *Surf. Sci. Rep.*, 1998, **31**, 235–325.
3 Q. Fu and T. Wagner, *Surf. Sci. Rep.*, 2007, **62**, 431–498.
4 D. P. Woodruff, *Chem. Rev.*, 2013, **113**, 3863–3886.
5 R. Lazzari and J. Jupille, *Surf. Sci.*, 2002, **507-510**, 683–687.
6 S. A. Chambers, T. Droubay, D. R. Jennison and T. R. Mattsson, *Science*, 2002, **297**, 827–831.
7 R. Lazzari and J. Jupille, *Phys. Rev. B*, 2005, **71**, 045409.
8 M. Messaykeh, J. Goniakowski, G. Cabailh, J. Jupille, R. Lazzari, P. Lagarde and N. Trcera, *J. Phys. Chem. C*, 2019, **123**, 29245–29254.
9 M. Messaykeh, S. Chenot, P. David, G. Cabailh, J. Jupille, A. Koltsov, P. Lagarde, N. Trcera and R. Lazzari, *Phys. Chem. Chem. Phys.*, 2021, **23**, 21852–21862.
10 N. Nilius, A. Corper, G. Bozdech, N. Ernst and H. Freund, *Prog. Surf. Sci.*, 2001, **67**, 99–121.
11 Y. Lei, F. Mehmood, S. Lee, J. Greeley, B. Lee, S. Seifert, R. E. Winans, J. W. Elam, R. J. Meyer, P. C. Redfern, D. Teschner, R. Schlogl, M. J. Pellin, L. A. Curtiss and S. Vajda, *Science*, 2010, **328**, 224–228.
12 M. Mannikko, X. Wang, M. Skoglundh and H. Harelind, *Appl. Catal., B*, 2016, **180**, 291–300.
13 S. L. Hemmingson and C. T. Campbell, *ACS Nano*, 2017, **11**, 4373.
14 J. van den Reijen, W. Versluis, S. Kanungo, M. d'Angelo, K. de Jong and P. de Jongh, *Catal. Today*, 2019, **338**, 31–39.
15 J. R. Smith and W. Zhang, *Acta Mater.*, 2000, **48**, 4395 – 4403.
16 H. Sadan and W. D. Kaplan, *J. Mater. Sci.*, 2006, **41**, 5099–5107.
17 G. Gluzer and W. D. Kaplan, *J. Eur. Ceram. Soc.*, 2013, **33**, 3101–3113.
18 N. Ni, Y. Kaufmann, W. D. Kaplan and E. Saiz, *Acta Mater.*, 2014, **64**, 282–296.
19 H.-L. T. Le, R. Lazzari, J. Goniakowski, R. Cavallotti, S. Chenot, C. Noguera, J. Jupille, A. Koltsov and J.-M. Mataigne, *J. Phys. Chem. C*, 2017, **121**, 11464–11471.
20 A. Kumar, H. Barda, L. Klinger, M. W. Finnis, V. Lordi, E. Rabkin and D. J. Srolovitz, *Nat. Commun.*, 2018, **9**, 5251.
21 M. Messaykeh, S. Chenot, P. David, G. Cabailh, J. Jupille, A. Koltsov and R. Lazzari, *Cryst. Growth Des.*, 2021, **21**, 3528–3539.
22 A. Khan, K. Balakrishnan and T. Katona, *Nat. Photonics*, 2008, **2**, 77–84.
23 Y. F. Chen, D. M. Bagnall, H. J. Koh, K. T. Park, K. Hiraga, Z. Q. Zhu and T. Yao, *J. Appl. Phys.*, 1998, **84**, 3912–3918.
24 T. Li, W. Guo, L. Ma, W. Li, Z. Yu, Z. Han, S. Gao, L. Liu, D. Fan, Z. Wang, Y. Yang, W. Lin, Z. Luo, X. Chen, N. Dai, X. Tu, D. Pan, Y. Yao, P. Wang, Y. Nie, J. Wang, Y. Shi and X. Wang, *Nat. Nanotechnol.*, 2021, **16**, 1201.
25 J. Wang, X. Xu, T. Cheng, L. Gu, R. Qiao, Z. Liang, D. Ding, H. Hong, P. Zheng, Z. Zhang, Z. Zhang, S. Zhang, G. Cui, C. Chang, C. Huang, J. Qi, J. Liang, C. Liu, Y. Zuo, G. Xue, X. Fang, J. Tian, M. Wu, Y. Guo, Z. Yao, Q. Jiao, L. Liu, P. Gao, Q. Li, R. Yang, G. Zhang, Z. Tang, D. Yu, E. Wang, J. Lu, Y. Zhao, S. Wu, F. Ding and K. Liu, *Nat. Nanotechnol.*, 2022, **17**, 33.
26 Y. Zhukovskii, E. Kotomin, B. Herschend, K. Hermansson and P. Jacobs, *Surf. Sci.*, 2002, **513**, 343–358.
27 C. Verdozzi, D. R. Jennison, P. A. Schultz and M. P. Sears, *Phys. Rev. Lett.*, 1999, **82**, 799–802.
28 A. Bogicevic and D. R. Jennison, *Phys. Rev. Lett.*, 1999, **82**, 4050–4053.
29 L. Xiao and W. F. Schneider, *Surf. Sci.*, 2008, **602**, 3445–3453.
30 S. Nigam and C. Majumder, *Langmuir*, 2010, **26**, 18776–18787.
31 S. Nigam and C. Majumder, *Appl. Surf. Sci.*, 2021, **547**, 149160.
32 W. Zhang and J. R. Smith, *Phys. Rev. Lett.*, 2000, **85**, 3225–3228.
33 D. J. Siegel, L. G. Hector and J. B. Adams, *Phys. Rev. B*, 2002, **65**, 085415.
34 J. Feng, W. Zhang and W. Jiang, *Phys. Rev. B*, 2005, **72**, 115423.
35 N. C. Hernández, J. Graciani, A. Márquez and J. F. Sanz, *Surf. Sci.*, 2005, **575**, 189 – 196.
36 J. R. B. Gomes, F. Illas, N. C. Hernández, A. Márquez and J. F. Sanz, *Phys. Rev. B*, 2002, **65**, 125414.
37 V. Rivanenkov, V. Nasluzov, A. Shor, K. Neyman and N. Rosch, *Surf. Sci.*, 2003, **525**, 173–183.
38 L. G. V. Briquet, C. R. A. Catlow and S. A. French, *J. Phys. Chem. C*, 2008, **112**, 18948–18954.
39 S. Nigam and C. Majumder, *J. Phys. Chem. C*, 2012, **116**, 2863–2871.
40 C. Rajesh, S. Nigam and C. Majumder, *Phys. Chem. Chem. Phys.*, 2014, **16**, 26561–26569.
41 S. Nigam and C. Majumder, *Appl. Surf. Sci.*, 2017, **422**, 1075–1081.
42 A. Beniya, N. Isomura, H. Hirata and Y. Watanabe, *Phys. Chem. Chem. Phys.*, 2014, **16**, 26485–26492.
43 E. Søndergård, O. Kerjan, C. Barreteau and J. Jupille, *Surf. Sci.*, 2004, **559**, 131–140.
44 S. Curiotto, H. Chien, H. Meltzman, P. Wynblatt, G. S. Rohrer, W. D. Kaplan and D. Chatain, *Acta Mater.*, 2011, **59**, 5320 – 5331.
45 Z. Fogarassy, G. Dobrik, L. K. Varga, L. P. Biró and J. L. Lábár, *Thin Solid Films*, 2013, **539**, 96 – 101.
46 C. Barth, A. S. Foster, C. R. Henry and A. L. Shluger, *Adv. Mater.*, 2011, **23**, 477–501.
47 A. Flank, R. Delaunay, P. Lagarde, M. Pompa and J. Jupille, *Phys. Rev. B*, 1996, **53**, R1737.
48 P. Lagarde, S. Colonna, A.-M. Flank and J. Jupille, *Surf. Sci.*,

2003, **524**, 102–112.
49 R. Lazzari, J. Goniakowski, G. Cabailh, R. Cavallotti, N. Trcera, P. Lagarde and J. Jupille, *Nano Lett.*, 2016, **16**, 2574–2579.
50 C. Mazzara, J. Jupille, A.-M. Flank and P. Lagarde, *J. Phys. Chem. B*, 2000, **104**, 3438–3445.
51 J. Jupille, A.-M. Flank and P. Lagarde, *J. Am. Ceram. Soc.*, 2002, **85**, 1041–1046.
52 P. Lagarde, A.-M. Flank, R. Prado, S. Bourgeois and J. Jupille, *Surf. Sci.*, 2004, **553**, 115–125.
53 G. Cabailh, J. Goniakowski, C. Noguera, J. Jupille, R. Lazzari, J. Li, P. Lagarde and N. Trcera, *Phys. Rev. Mater.*, 2019, **3**, 046001.
54 C. R. Cammarata, *Progr. Surf. Sci.*, 1994, **46**, 1.
55 V. Bonačić-Koutecky, V. Veyret and R. Mitrić, *J. Chem. Phys.*, 2001, **115**, 10450–10460.
56 R. Fournier, *J. Chem. Phys.*, 2001, **115**, 2165–2177.
57 R. Lazzari and J. Jupille, *Nanotechnology*, 2012, **23**, 135707.
58 P. Horta-Fraijo, M. Cortez-Valadez, N. Flores-Lopez, R. Britto Hurtado, R. Vargas-Ortiz, A. Perez-Rodriguez and M. Flores-Acosta, *Phys. E: Low-Dimens. Syst. Nanostructures*, 2018, **97**, 111–119.
59 D. A. Ryzhkova, S. L. Gafner and Y. Y. Gafner, *JETP Lett.*, 2021, **113**, 638 – 645.
60 Y. Gafner, S. Gafner and D. Bashkova, *J. Nanopart. Res.*, 2019, **21**, 243.
61 R. Lazzari, J. Jupille, R. Cavallotti, E. Chernysheva, S. Castilla, M. Messaykeh, Q. Hérault, I. Gozhyk and E. Meriggio, *ACS Appl. Nano Mater.*, 2020, **3**, 12157–12168.
62 I. Simonsen, R. Lazzari, J. Jupille and S. Roux, *Phys. Rev. B*, 2000, **61**, 7722–7733.
63 R. Lazzari, I. Simonsen, D. Bedeaux, J. Vlieger and J. Jupille, *Eur. Phys. J. B*, 2001, **24**, 267–284.
64 R. Lazzari and J. Jupille, *Nanotechnology*, 2011, **22**, 445703.
65 W. Winterbottom, *Acta Metall.*, 1967, **15**, 303–310.
66 K.-I. Shimizu, K. Sugino, K. Sawabe and A. Satsuma, *Chem. Eur. J.*, 2009, **15**, 2341–2351.
67 A. S. Crampton, M. D. Rötzer, C. J. Ridge, B. Yoon, F. F. Schweinberger, U. Landman and U. Heiz, *Surf. Sci.*, 2016, **652**, 7–19.
68 D. Vantelon, N. Trcera, D. Roy, T. Moreno, D. Mailly, S. Guilet, E. Metchalkov, F. Delmotte, B. Lassalle, P. Lagarde and A.-M. Flank, *J. Synchrotron Radiat.*, 2016, **23**, 635–640.
69 C. T. Campbell and S. M. Valone, *J. Vac. Sci. Technol. A*, 1985, **3**, 408–411.
70 J. Goniakowski, F. Finocchi and C. Noguera, *Rep. Prog. Phys.*, 2008, **71**, 016501.
71 R. Cavallotti, J. Goniakowski, R. Lazzari, J. Jupille, A. Koltsov and D. Loison, *J. Phys. Chem. C*, 2014, **118**, 13578–13589.
72 P. Guénard, G. Renaud, A. Barbier and M. Gautier-Soyer, *Surf. Rev. Lett.*, 1998, **5**, 321.
73 G. Renaud, *Surf. Sci. Rep.*, 1998, **32**, 1–90.
74 B. Ravel and M. Newville, *J. Synchrotron Radiat.*, 2005, **12**, 537–541.
75 O. Robach, G. Renaud and A. Barbier, *Phys. Rev. B*, 1999, **60**, 5858–5871.
76 G. Kresse and J. Furthmuller, *Phys. Rev. B*, 1996, **54**, 11169–11186.
77 G. Kresse and J. Hafner, *Phys. Rev. B*, 1993, **47**, 558–561.
78 P. E. Blöchl, *Phys. Rev. B*, 1994, **50**, 17953–17979.
79 G. Kresse and D. Joubert, *Phys. Rev. B*, 1999, **59**, 1758–1775.
80 K. Momma and F. Izumi, *J. Appl. Crystallogr.*, 2011, **41**, 1272–1276.
81 J. P. Perdew, A. Ruzsinszky, G. I. Csonka, O. A. Vydrov, G. E. Scuseria, L. A. Constantin, X. Zhou and K. Burke, *Phys. Rev. Lett.*, 2008, **100**, 136406.
82 B. Simard, P. A. Hackett, A. M. James and P. R. R. Langridge-Smith, *Chem. Phys. Lett.*, 1991, **186**, 415–422.
83 M. Dion, H. Rydberg, E. Schroder, D. C. Langreth and B. I. Lundqvist, *Phys. Rev. Lett.*, 2004, **92**, 246401.
84 J. Klimes, D. R. Bowler and A. Michaelides, *J. Phys.: Cond. Matt.*, 2010, **22**, 022201.
85 J. Klimes, D. R. Bowler and A. Michaelides, *Phys. Rev. B*, 2011, **83**, 195131.
86 S. Prada, L. Giordano, G. Pacchioni and J. Goniakowski, *Appl. Surf. Sci.*, 2016, **390**, 578–582.